PAPER • OPEN ACCESS

Electrode fabrication and interface optimization for imaging of evoked peripheral nervous system activity with electrical impedance tomography (EIT)

View the article online for updates and enhancements.

IOP ebooks™

Bringing you innovative digital publishing with leading voices to create your essential collection of books in STEM research.

Start exploring the collection - download the first chapter of every title for free.

Electrode fabrication and interface optimization for imaging of evoked peripheral nervous system activity with electrical impedance tomography (EIT)

Christopher A R Chapman[1,4], **Kirill Aristovich**[1], **Matteo Donega**[2], **Cathrine T Fjordbakk**[3], **Thaleia-Rengina Stathopoulou**[3], **Jaime Viscasillas**[3], **James Avery**[1], **Justin D Perkins**[3] **and David Holder**[1]

[1] Department of Medical Physics and Biomedical Engineering, University College London, Gower Street, London WC1E 6BT, United Kingdom
[2] Galvani Bioelectronics, Neuromodulation Devices Team, Stevenage, HERTS SG1 2NY, United Kingdom
[3] Department of Clinical Science and Services, The Royal Veterinary College, Hatfield AL9 7TA, United Kingdom

E-mail: christopher.chapman@ucl.ac.uk

CrossMark

Abstract

Objective. Non-invasive imaging techniques are undoubtedly the ideal methods for continuous monitoring of neural activity. One such method, fast neural electrical impedance tomography (EIT) has been developed over the past decade in order to image neural action potentials with non-penetrating electrode arrays. *Approach*. The goal of this study is two-fold. First, we present a detailed fabrication method for silicone-based multiple electrode arrays which can be used for epicortical or neural cuff applications. Secondly, we optimize electrode material coatings in order to achieve the best accuracy in EIT reconstructions. *Main results*. The testing of nanostructured electrode interface materials consisting of platinum, iridium oxide, and PEDOT:pTS in saline tank experiments demonstrated that the PEDOT:pTS coating used in this study leads to more accurate reconstruction dimensions along with reduced phase separation between recording channels. The PEDOT:pTS electrodes were then used *in vivo* to successfully image and localize the evoked activity of the recurrent laryngeal fascicle from within the cervical vagus nerve. *Significance*. These results alongside the simple fabrication method presented here position EIT as an effective method to image neural activity.

Keywords: electrical impedance tomography, neural recording, peripheral nerve cuff, electrode characterization, laser-based fabrication

Introduction

Development and advancements in the design and fabrication of silicone elastomer-based electrode arrays has led to significantly improved performance for many implantable devices. This has been predominantly attributed both to the low elastic modulus of the silicone elastomer that leads to less material mismatch between the tissue and implant [1]. Due to these beneficial properties, the field of neuroscience has recently seen an influx of implanted electrode arrays which take advantage of these material properties for improved recording fidelity [2–9]. For example, stretchable penetrating electrode arrays have shown significant improvements in signal-to-noise ratio for *in vivo* electrophysiological recordings due to

a decreased level of chronic scar tissue formation due to the implant flexing with the tissue motion [1, 10]. Non-penetrating electrode arrays, such as epicortical [11] and neural cuff arrays [12, 13], benefit from improved shape conformation to the cortex and nerve respectively due to their low elastic modulus [1]. Due to the ease of implantation and recent trend towards developing next-generation neural cuff electrodes the majority of the currently utilized implants in the peripheral nervous system are non-penetrating neural cuff arrays.

Despite the benefits gained by utilizing non-penetrating elastomer-based implants, recording electrical activity from the peripheral nervous system remains challenging due to physiological barriers, such as connective tissue and the epineurium [14], which isolate the nerve fibers from the electrodes. Additionally, temporal dispersion of nerve activity due to differing fiber sizes creates a unique challenge in recording information from the long peripheral nerves in large animals [15]. Recently, aided by the implantation of surface conforming elastomer-based arrays, electrical impedance tomography (EIT) has shown promise as a technique that can move beyond the limitations of non-penetrating electrodes to image and localize changes in neural activity within peripheral nerves caused by downstream electrical stimulation [16]. However, due to the small changes in signal recorded during EIT, significant attention must be given to designing an adequate neural interface that outperforms commercially available electrode arrays.

EIT is a method in which changes of the electrical properties in a volume can be reconstructed using only surface electrodes. Measurements are carried out by injecting a current between a pair of electrodes and recording the resulting voltages on the other electrodes. This process is repeated multiple times by quickly switching between injecting electrodes [17]. The resulting data is then reconstructed using a finite element model (FEM) to visualize the distribution of conductivity in the domain. Its principal application has been in imaging relatively large impedance changes which occur during lung ventilation [18]; however the ability to image the small impedance changes which is hypothesized to result from ion channel opening in neurons has been demonstrated multiple times [16, 19]. This technique has permitted imaging of functional neural activity over milliseconds with a resolution of approximately 200 μm in the cerebral cortex and peripheral nerve in rats [19–21]. The impedance changes measured from neuron depolarization are approximately 1%–0.1% of the domain background impedance making high performance working electrode areas a key functional part of the EIT system. In each of these previous studies, non-electrochemically characterized platinum electrodes ranging from 0.11 to 0.28 mm^2 in geometric area were utilized, potentially leading to low signal-to-noise ratio and thus less accurate recordings. Therefore, in order to optimize imaging accuracy new electrode materials for EIT imaging must be considered. Ideal electrode interfaces for EIT would incorporate materials that have large surface area to achieve consistent low impedance (less than 5% variation between electrodes) while maintaining low geometrical area (for increased special resolution). Additionally, the EIT electrodes must be able to both record and stimulate without

significantly damaging the interface surface, a requirement than can be achieved through choosing material that are proven to be compatible with electrical stimulation [22, 23].

The purpose of this work was two-fold. First, a simple method for the reproducible fabrication of textured elastomer-based electrode arrays that can be used as both epicortical mats and neural cuffs was developed. Secondly, we characterized and designed the electrode interface materials such that the properties specific to EIT were optimized.

Experimental design

Here we present a detailed method for the rapid fabrication of medical grade silicone embedded stainless-steel electrode arrays and the subsequent deposition of platinum, iridium oxide, and PEDOT:pTS onto the electrode surfaces. The electrochemical performance of material was characterized for performance in EIT recordings with a focus on impedance reduction, phase stability, and increased charge storage capacity in comparison to previously utilized platinum electrodes. The effectiveness of each material as electrodes for EIT was tested using a saline filled tank with a large known impedance change. The accuracy of the reconstructed images for each electrode material and the phase stability of each material were assessed with metrics of shape and positional error. Finally, in accordance with Home Office animal reduction practices a single material was chosen to test *in vivo* through a combination of electrochemical data and *in vitro* reconstruction accuracy. To demonstrate the efficacy of the improved electrode coating in an *in vivo* setting we recorded and reconstructed functional activity from stimulated compound action potentials of the recurrent laryngeal nerve from a cuff around the right cervical vagus nerve of a sheep.

Materials and methods

Fabrication of electrode array cuffs

The electrode arrays used in this study were fabricated using an eight step process (figure 1). First, 52 × 76 mm glass slides (Fisher Scientific UK) were cleaned with isopropanol (VWR International, UK), spin-coated with a lift-off layer of poly-styrenesulfonic acid (PSSA) at 200 RPM for 10 s followed by 4000 RPM for 45 s, and subsequently dried for 5 min at 150 °C. An approximately 30 μm-thick layer of silicone (NuSil MED4-4220, Polymer Systems UK) was spun onto the PSSA layer using the same parameters as the PSSA. Samples were cured at 100 °C for 3 min. A solid 12.5 μm-thick stainless-steel foil (Advent Inc) was rolled onto the surface of the silicone. Using a laser cutter (Nd:YAG Class IV laser, Laservall S.p.A., Italy), the outlines for the electrode and traces were cut with a power of 40%, a shot frequency of 4000 Hz, and a speed of 3.1 mm s^{-1}. The excess material was removed by hand. Next, a layer of silicone, dyed black (NuSil MED51-4800-2, Polymer Systems UK), was spun to approximately 30 μm-thick using the same spinning parameters as above and cured at 100 °C for 30 min. The electrode openings were exposed by selectively
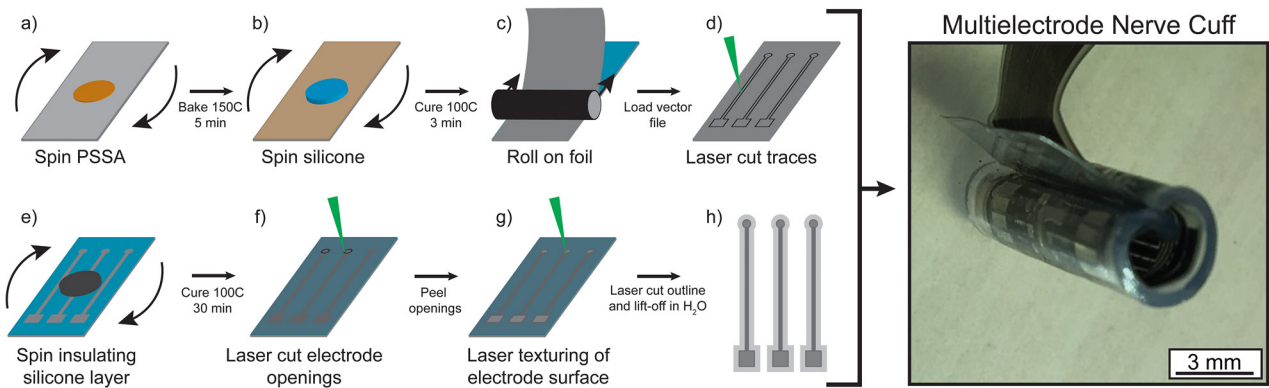
Figure 1. Fabrication work flow images and images of the final arrays. (a) Spinning of PSSA lift-off layer; (b) spinning of bottom silicone insulation layer; (c) application of stainless-steel foil; (d) laser cutting of metal traces; (e) spinning of top silicone insulation layer; (f) laser cutting of electrode openings; (g) laser texturing of electrode surfaces; and (h) laser cutting of device outline and lifting off in deionized water. Far right shows an image of the fully fabricated cuffed electrode array.

cutting the top layer of silicone with the laser at a power of 40%, a shot frequency of 10 000 Hz, and a speed of 10 mm s^{-1} with four passes. The redundant silicone was removed by hand. The exposed electrode surfaces were roughened using laser ablation at 40% power, a shot frequency of 10 000 Hz, and a speed of 10 mm s^{-1} (only one pass) to increase the initial starting surface area of the electrodes as well as to clear specific defect areas that could cause inconsistent charge distribution. Finally, the outline of the device was cut and each array lifted off using deionized water.

Electrodeposition of electrode materials

Prior to deposition, all electrode surfaces were prepared as follows. First, the electrodes were immersed for 30 s into ethanol (VWR International, UK), then transferred to 37% hydrochloric acid (VWR International, UK) for 30 s to clean the surface of contaminants. Electrodes were then washed in deionized water for 30 s before immersion in the plating bath. Three electrode materials were tested: (1) Platinum black was deposited by immersion of the electrodes in a 4% chloroplatinic acid solution (Sigma Aldrich) and application of cathodal direct current with a density of 21.5 mA cm^{-2}. Four cycles of 60 s positive and 60 s negative current were used. (2) PEDOT:pTS was deposited through immersion of the electrodes in a plating solution containing 100 mM 3,4-ethylenedioxythiophene (EDOT) and 50 mM sodium p-toluenesufonate (Sigma Aldrich) in a 1:1 dilution of acetonitrile (VWR International, UK) and deionized water. Electrodes were plated with 2 mA cm^{-2} cathodal direct current for 450 s. (3) Iridium oxide was deposited by immersion of the electrodes in a plating solution made following the protocol outlined in Hu *et al* [24]. The plating was done through 600 cycles of cyclic voltammetry scans between -0.8 and $+0.7$ V, compared to an Ag/AgCl reference (Sigma Aldrich), at 0.1 V s^{-1}. After the plating of each material, the array was washed with deionized water for 1 min in a 25 ml bath to ensure no residual plating solutions were left on the silicone insulation. All depositions were performed using a PalmSens4 potentiostat (PalmSens, Netherlands) and a 3 × 12 mm platinum plate counter electrode.

Electrochemical measurements

All electrical impedance spectra measurements were made using a PalmSens four potentiostat with a platinum wire counter electrode and an Ag/AgCl reference dimensions in 0.9% saline. Charge storage capacity was calculated from cyclic voltammetry measurements between -0.7 and 0.7 V compared to the Ag/AgCl reference by using MATLAB to estimate the area of the CV curve using trapezoidal area estimation. All the active electrode sites ($n = 28$) on a single cuff ($N = 1$) electroplated with a given material (platinum, iridium oxide, or PEDOT:pTS) were used to make 28 electrochemical measurements for each material tested in this study.

Scanning electron microscopy

Electrode surface morphologies before and after deposition of each material were characterized visually with a Zeiss EVO MA10 scanning electron microscope.

Electrical impedance tomography (EIT)

EIT data was collected through a custom-built controller and switch connected to a commercial EEG amplifier system (ActiChamp) [25]. Current injection was performed with a standard commercial current source (Keithly 6221, US). The recorded raw voltages on all electrodes were converted to absolute impedance traces through the application of a 3rd order bandpass filter followed by a Hilbert transform resulting in the modulated envelope of the injected sine wave. Time-difference EIT images were then reconstructed from the absolute impedance traces calculated from each surrounding electrode using a two-step reconstruction process. A total of 91 independent measurements were used to reconstruct each image. First, a forward problem was defined with a cylindrical mesh with a 3 mm diameter with the appropriate electrode sites predefined as per the locations of the electrodes in a cuff. The forward problem was computed using an electrode model with the UCL PEIT forward solver [26]. The electrode contact impedances in this model were changed according to their measured real impedance in 0.9% saline (see results for
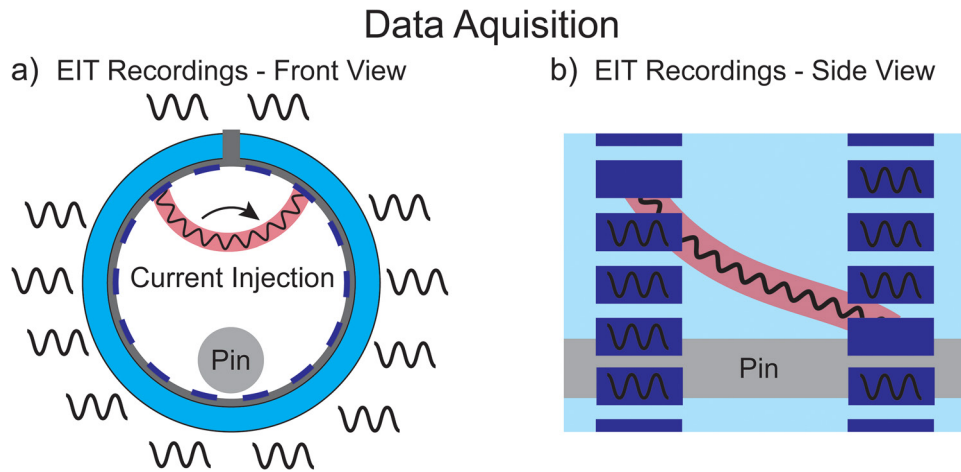
Data Aquisition

a) EIT Recordings - Front View

b) EIT Recordings - Side View

Figure 2. Schematic of a single recording of EIT data from an injection pair in both (a) front and (b) side view. The injection pair was then switched between the other electrodes to gather a full data set.

exact numbers used). Second, Jacobian matrix inversion was accomplished using 0th order Tikhonov regularization and processed using noise-based voxel correction [21]. The |dZ| data at each 0.01 ms interval was then reconstructed onto a hexahedral mesh of the same overall dimensions of the nerve using the same algorithm as previously reported for peripheral nerves [16]. Each voxel was divided by the standard deviation of the noise resulting in a normalized value of conductivity change (Z-score—arbitrary units) in each voxel with respect to the background noise.

EIT of metal pin in saline

Electrode arrays were fabricated into 3 mm diameter neural cuffs with 28 0.466×3 mm active electrode sites and submerged into 0.9% saline solution (Animalcare Aqupharm one physiological saline) at 25 °C with an impedance of approximately 85.5 kΩ. An approximately 32 500-fold impedance change was simulated by the insertion of a 1 mm diameter stainless-steel pin with an impedance of approximately 2.5 Ω into the submerged cuff. Although impedance changes above 20% may be non-linear, the metal pin provided a strong, assured signal as a baseline in which to compare different electrode materials, similar to the contrast used in lung EIT [27]. EIT recordings were performed, with the stainless-steel pin present and without the stainless-steel pin as a reference to form a differential measurement of impedance decrease, by injecting a 100 μA current at a frequency of 9 kHz across the array between electrodes 90° from each other on the array and simultaneously recording voltages at a 100 kHz sampling rate on every other electrode in the array. The injecting pair was then switched at an interval of 10 s and the measurements repeated six times for a total of 14×6 recordings and a total time of 14 min (figure 2).

The EIT recordings were then used to reconstruct images of the volume conductance (i.e. impedance changes) using methods stated above. Average diameter and circularity (scale from 1 to 0 with 1 being a perfect circle) were calculated through thresholding via ImageJ. The average phase shift was calculated in MATLAB by computing the difference between the reference (injected current) phase and the phase on all other electrodes. This was repeated for each injection leading to 6 sets of 14 averages for each material (per electrode ring).

Animal preparation

All experimental procedures complied with regulations in the UK Animal (Scientific Procedures) Act, 1986 and were approved by the University Ethics and Welfare Committee. Adult female English mule sheep four years of age, bodyweight 70–80 kg, were anaesthetized using ketamine (5 mg kg^{-1}) and midazolam (0.5 mg kg^{-1}) administered intravenously. Animals were then intubated with an endotracheal tube, and anaesthesia was maintained by positive pressure ventilation with sevoflurane inhalant vaporized in a mixture of oxygen and medical air. Mechanical ventilation was maintained for surgery and implantation, after which animals were restored to spontaneous breathing. Anaesthesia monitoring included pulse oximetry, capnograph, electrocardiogram, invasive arterial blood pressure, central venous pressure and respiratory gas analysis.

Animals were positioned in dorsal recumbency, and the ventral neck was clipped and aseptically prepared and draped in a routine fashion. Using aseptic technique, a 15 cm longitudinal skin incision was made immediately to the right of the trachea, commencing at the larynx and extending caudad. The incision was continued through the subcutaneous tissues and blunt dissection commenced between the muscle planes until encountering the carotid sheath and the right cervical vagus nerve. By careful dissection, a 6 cm segment of the nerve was circumferentially isolated from surrounding fat and loose connective tissue. The fabricated cuff was then implanted around the nerve by grasping one end of the cuff with forceps and pulling under the nerve until it was fully surrounding the nerve. The right recurrent laryngeal nerve was then identified, and a 2 cm segment was isolated as described above and placed onto silver chloride hook electrodes. Electrical ground electrodes were inserted into the surgical field. At the end of the experiment, animals were humanely euthanized with an overdose of pentobarbital administered intravenously.

EIT of recurrent laryngeal nerve

Using silver chloride hook electrodes sealed with Kwik-Sil (WPI Inc.) the recurrent laryngeal nerve was stimulated at a frequency of 20 Hz and a pulse width of 250 μs causing sustained compound activity. A 30 channel EIT cuff was implanted onto the right cervical vagus nerve of an anaesthetized sheep using the protocol outlined above. EIT data was collected with 14 different injecting electrode pairs across the array. EIT recordings were carried out by injecting a 200 μA current at a frequency of 9 kHz between electrodes 90° from each other on the array and simultaneously recording voltages at a 100 kHz sampling rate on every other electrode in the array. The injecting pair was then switched between each 90° pair of electrodes (figure 2) at an interval of 30 s and the measurements repeated. With the stimulation rate of 20 Hz the total number of trials was 600 for each injecting pair, resulting in 7 min to collect the dataset of 364 averaged dZ traces lasting 50 ms each. The recorded EIT data set was then reconstructed into a volume conductance change of the right vagus nerve over time using the methods presented above and the frame before stimulation as the reference measurement. Regions of interest were defined from the mesh used to reconstruct the data and used to calculate the average value over time with MATLAB. The area and center of mass of the reconstructed area was calculated using ImageJ.

Statistical analysis

All reported values are averages with error bars corresponding to one standard deviation unless otherwise stated. A two-tailed Student's *t*-test assuming unequal variance was used to identify differences between two different samples groups. Statistical significance was determined by *p*-values < 0.05.

Results

Characterization of electrode arrays

Using the above fabrication method, arrays consisting of 30 electrodes (28 active sites with a geometry of 0.466×3 mm and 2 reference sites with a geometry of 0.4×10 mm) were made (figure 3(a)). Each electrode in the array was then electroplated with either platinum, iridium oxide, or PEDOT:pTS following the protocols outlined in the methods section. Scanning electron microscope images of the electrode surfaces after coating show the uniformity and overall microstructure of the deposited coatings (figure 3(b)).

In order to assess the electrochemical performance of the coated materials, impedance spectra and charge storage capacity were characterized for each electrode material. There were significant improvements of each deposited coating on both the real impedance and phase in comparison to the bare stainless-steel electrodes ($p < 0.05$ for all coatings; $n = 28$ separate electrode repeats in $N = 1$ single cuff). The lowest impedance was achieved with PEDOT:pTS at 297 ± 1.04 Ω at 1 kHz followed closely by iridium oxide at 340 ± 1.02 Ω at 1 kHz (figure 4(a)). These two materials also demonstrated the lowest phase shift with $1.53 \pm 0.31°$ at 1 kHz for PEDOT:pTS and $1.01 \pm 0.38°$ at 1 kHz for iridium oxide (figure 4(b)). Platinum coated electrodes, although significantly better than stainless-steel, only achieved a real impedance of 377 ± 1.02 Ω and a phase shift of $4.35 \pm 0.37°$ at 1 kHz which were worse than either PEDOT:pTS or iridium oxide respectively. Additionally, both the PEDOT:pTS and iridium oxide coatings displayed significantly higher charge injection capacity throughout 800 cyclic voltammetry cycles that platinum. However, as demonstrated in other research [28], the PEDOT:pTS coatings did have an approximately 40% reduction in CSC over the 800 cycles from 265 to 149 μC cm^{-2} whereas iridium oxide demonstrated no degradation and instead showed an increase of CSC over the 800 cycles from 99 to 130 μC cm^{-2} (figure 4(c)).

Validation and characterization of EIT recording in saline solution

In order to validate the efficacy of each electrode material in imaging with EIT, an approximately 32 500-fold negative impedance change of 1 mm in diameter was imaged. Although typical impedance changes of neural tissue are small (1%–0.1%), a large impedance change was used for this validation in order to ensure an easily visible image could be reconstructed to analyze the accuracy of the images from each material type.

These reconstructions show that all three coating materials can visualize the large impedance change of a metal pin versus a 0.9% saline solution (figure 5(a)). Images acquired with PEDOT:pTS and platinum more accurately represent the true radius of the metal pin (0.53 and 0.46 mm respectively), whereas the circularity of the metal pin was captured only by the iridium oxide and PEDOT:pTS (0.72 and 0.62 respectively) (figure 5(b)). Additionally, the scale of Z-score (synonymous with signal-to-noise ratio) shows that PEDOT:pTS and iridium oxide have a maximum reconstruction SNR 1.43 and 1.91-fold higher than platinum.

Another key source of image accuracy when recording neural activity with EIT is the consistency of phase between recording electrodes. The analysis method used to extract the impedance signal from the raw voltages assumes there are changes in only real impedance. Therefore, if the phase shift is bigger than several degrees there can be errors in estimation of the real part of the impedance change. To assess the performance of the electrode surfaces, data from the saline tank experiments was used to calculate the phase lag between each electrode was compared with respect to the injecting electrode (figure 6(a)). This comparison was made for each injection resulting in 6 averages for each of the 14 active electrode sites in a single ring ($N = 14$, $n = 84$).

In phase measurements compared to injected current, the phase shifts were $1.02 \pm 0.28°$, $0.49 \pm 0.18°$, $0.93 \pm 0.47°$ for iridium oxide, PEDOT:pTS, and platinum respectively. The PEDOT:pTS electrodes demonstrated a significantly ($p < 0.05$) lower phase shift compared to either iridium oxide or platinum (figure 6(b)). The assessment of reconstruction
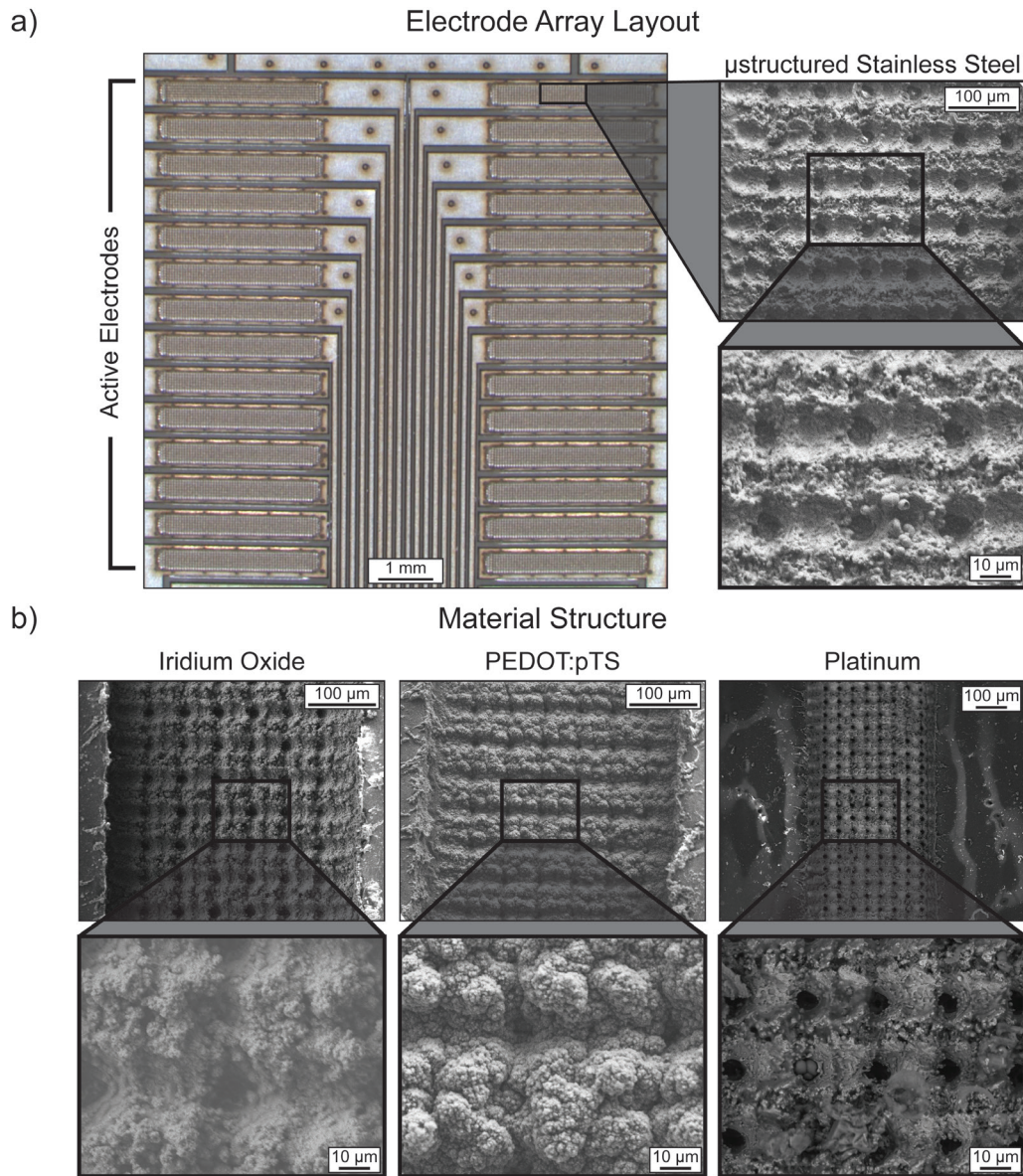
a)
Electrode Array Layout

Figure 3. (a) Bright field microscope image of the uncuffed electrode surface illustrating the 28 active electrode sites. Scanning electron microscope images of the laser roughened stainless-steel electrode surfaces clearly demonstrate the uniformity of the roughening pattern. (b) Low and high magnification scanning electron microscope images of the electrochemically deposited layers show the overall uniformity and microstructural differences between materials.

accuracy (figures 5(a) and (b)), shows that PEDOT:pTS and iridium oxide coated electrodes provide the best signal-to-noise ratio in the reconstruction of EIT images compared to platinum. Alongside the improved phase shift with respect to the injected current demonstrated by PEDOT:pTS (figure 6(b)), we moved forward with *in vivo* experiments using this material.

Characterization of PEDOT:pTS cuffs in vivo

In order to examine the efficacy of PEDOT:pTS coated electrode arrays in measuring fast neural activity, neural cuffs were fabricated with exactly the same dimensions as used in the tank experiments and used *in vivo*. The multielectrode cuff (labeled EIT Cuff in figure 7(a)) was implanted around the right cervical vagus nerve of an anaesthetized sheep as

described above. A pair of stimulating electrodes (silver chloride hook electrodes) were implanted around the exposed right recurrent laryngeal nerve and sealed with silicone (figure 7(a)). The recurrent laryngeal nerve primarily carries motor innervation to the larynx and travels together with the cervical vagus nerve before it splits under the carotid artery. Since the recurrent laryngeal nerve is predominantly responsible for carrying motor signals it is predominantly comprised of fast neural fibers (i.e. A-alpha fibers) [29]. Supramaximal electrical stimulation was applied to the recurrent laryngeal nerve while the fabricated multielectrode cuff was used to image the vagus nerve using EIT. This yielded a compound action potential approximately 8–10 ms after stimulation (figure 7(b)). The conduction velocity (~100 m s^{-1}) of this activity caused by the stimulation of the recurrent laryngeal nerve matches the expected conduction velocity of the predominant fiber type
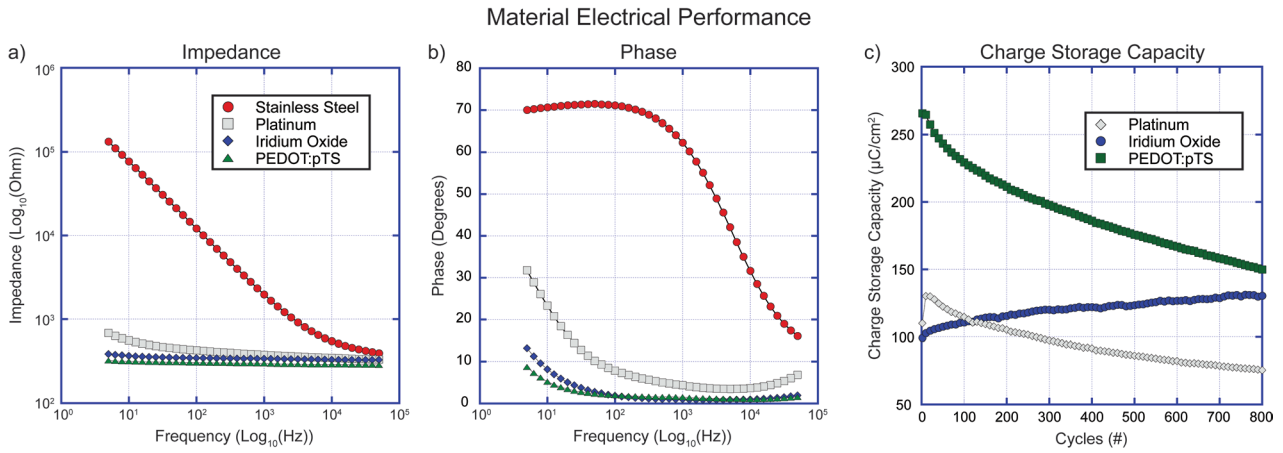
Figure 4. (a) Real impedance for each electrode material (including stainless-steel) on a 1.05 mm² area electrode opening. PEDOT:pTS (green) and iridium oxide (blue) clearly demonstrate the lowest values compared to both platinum and stainless-steel over the entire frequency spectrum. (b) Phase shift for each electrode material (including stainless-steel). PEDOT:pTS and iridium oxide again demonstrate significantly lower phase shift across the entire frequency spectrum. (c) Quantification of charge storage capacity (CSC) for each electrode material over 800 cyclic voltammetry cycles from -0.7 to 0.7 V. Although PEDOT:pTS started with a significantly higher CSC than either iridium oxide or platinum, after 800 cycles decrease in CSC brings it closer to that of iridium oxide.
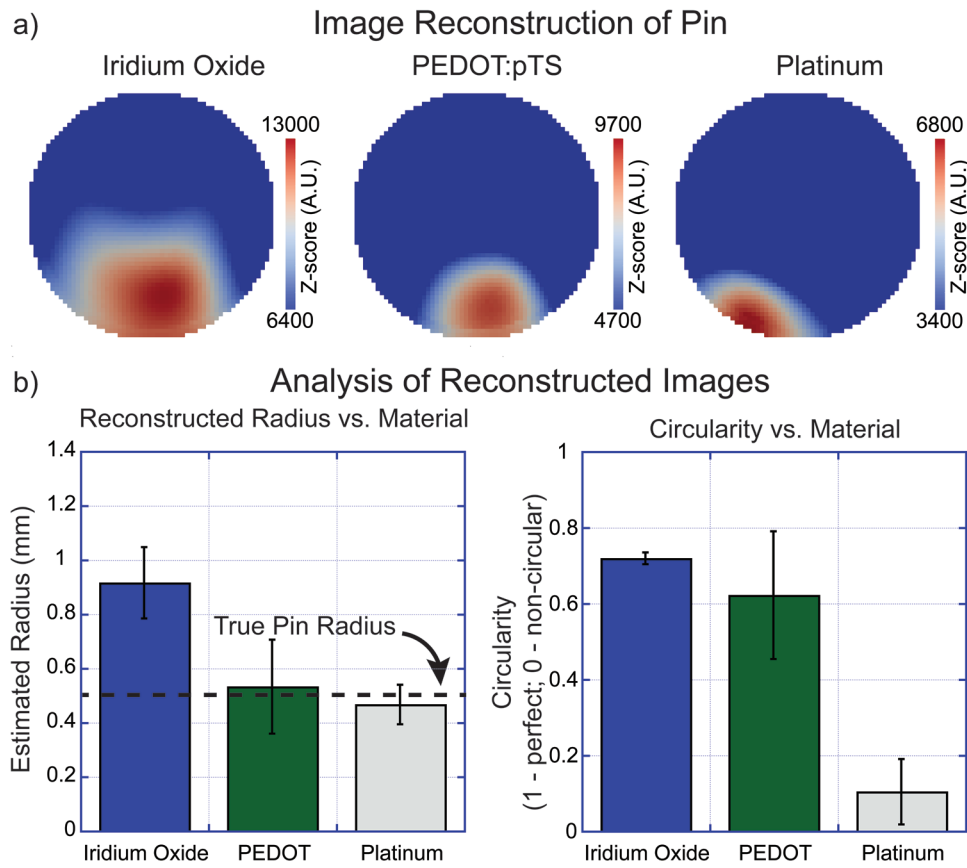

Figure 5. (a) Reconstructed images of the changes in volume conductivity caused by a 1 mm diameter metal pin as imaged by each individual electrode material. (b) Analysis of the reconstructed images demonstrated that while PEDOT:pTS and iridium oxide estimated the circularity of the pin, PEDOT:pTS and platinum were more accurate in representing the true pin radius. Error bars show one standard deviation.

(A-alpha) that constitutes the nerve in humans [30]. Further analysis of the recorded EIT data revealed a distinct impedance change directly correlating to the timing of the compound action potential of the recurrent laryngeal nerve (figure 7(b)).

A volume impedance change corresponding to the timing of the compound action potential from the stimulated recurrently laryngeal nerve can be seen in the bottom right of the reconstructed images (figure 7(c)). In order to demonstrate this
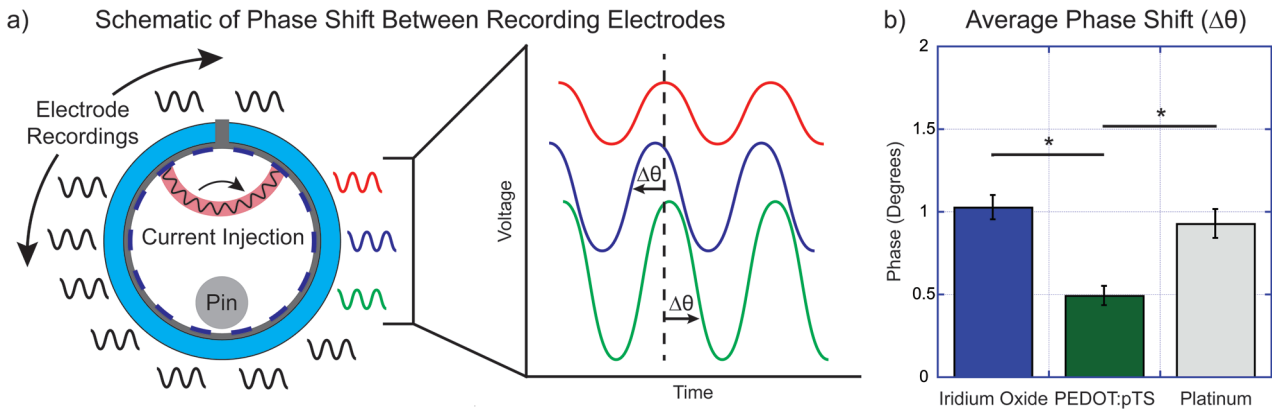
Figure 6. (a) Schematic of the comparison of phase lag between the recorded voltages on each electrode during an EIT current injection. This comparison was done across all injections for each electrode. (b) Calculated average phase shift for each recording electrode through an entire EIT data set show PEDOT:pTS maintains significantly lower average phase shift between electrodes than either iridium oxide or platinum. Error bars show standard deviation. Horizontal bars with an asterisk signify statistical significance ($p < 0.05$).

more accurately, an average conductance value over time was taken from two regions of interest in the reconstructed images. The comparison of average conductivity between regions of interest with (green) and without neural activity (black) shows the high specificity of the neural activity through time (figure 7(c)). Average area and center of mass analysis for repeats on individual animals ($n = 6$ from $N = 2$ sheep) reveal an average area of 2.36 ± 0.44 and $0.43 \pm 0.11 \, mm^2$ with centers of mass at $(2.13 \pm 0.08 \, mm, \ 2.4 \pm 0.1 \, mm)$ and $(2.25 \pm 0.67 \, mm, 1.04 \pm 0.1 \, mm)$ respectively for the animals tested.

Discussion

The laser-based fabrication method used in this study is built on the foundation of many other publications utilizing similar methods [31, 32]. Here, we have used those methods in conjunction with the surface texturing of electrodes, another technique used to improve deposition uniformity [33], to produce low impedance silicone multiple electrode arrays for the application of fast neural EIT.

The simple fabrication of these electrode arrays enabled the testing of multiple electrodeposited coatings to optimize the properties of the recording and stimulating electrodes. In this work we utilized three materials, platinum, iridium oxide, and PEDOT:pTS all which have been widely used for improving the performance of electrodes [28, 34–38]. Although each of these materials have been widely utilized for improving electrical recording and stimulating electrodes, only platinum has been used specifically in the application of EIT [20]. Although evaluated solely on a known impedance phantom, this work presents the first direct comparison between electrode coatings and their efficacy in EIT. These phantom experiments were used to select PEDOT:pTS as the best candidate for moving forward with *in vivo* imaging. This is attributed to the simplicity of PEDOT:pTS deposition and the improved accuracy in EIT reconstructions compared to both platinum and iridium oxide make it an ideal choice for electrodes to record fast neural activity with EIT. This is attributed to the consistent low impedance, improved charge injection capabilities, ease

of deposition, and reduced phase separation between electrodes that PEDOT:pTS offers. Although the electrodeposited iridium oxide coating also performed adequately for stability and EIT reconstruction, the electrodeposition of iridium oxide is not the most effective way to form a high performance iridium oxide layer. Other methods such as sputtered iridium oxide or activated iridium oxide have been shown to form significantly better performing layers [39]. Therefore, iridium oxide coated electrodes could potentially be optimized to match or exceed the PEDOT:pTS coating through additional microfabrication steps. Additionally, although alterations to the overall nerve cuff geometry were not investigated here, there are many studies showing the efficacy of non-circular or flat geometries [40]. Utilizing a cuff with this geometry could potentially enhance the localization ability of EIT even further by minimizing the volume between individual electrodes.

Over the past five years, EIT has been demonstrated as one of the few techniques available for the non-invasive imaging of evoked neural activity inside a volume. This has been demonstrated in the rat cortex with epicortical mat arrays [20] as well as in a peripheral nerve model of the crab walking leg [41] and rat sciatic [16]. Although measurement of EIT uses an applied current, this current is significantly lower than what is needed to cause neural activity. In addition to this current being orders of magnitude less than the threshold of activation for neural tissue [42], in these experiments we see that: (1) the evoked CAP is unmodified before versus during injection; and (2) physiological parameters such as EEG, blood pressure, and end tidal CO_2 do not change during EIT versus before. In this work we show that nerve cuffs with the optimized PEDOT:pTS coating were able to localize impedance changes corresponding to observed compound activity that was likely originating from the motor fibers in the recurrent laryngeal nerve. The timing of the compound action potential at approximately 8–10 ms after stimulation over a distance of approximately 1 meter suggests that the fibers imaged here are A-alpha motor fibers with a conduction velocity in the realm of 100–120 m s^{-1}, a result which is consistent with previous histological studies of the recurrent laryngeal nerve [30, 43]. The reconstructed images were consistent across two separate
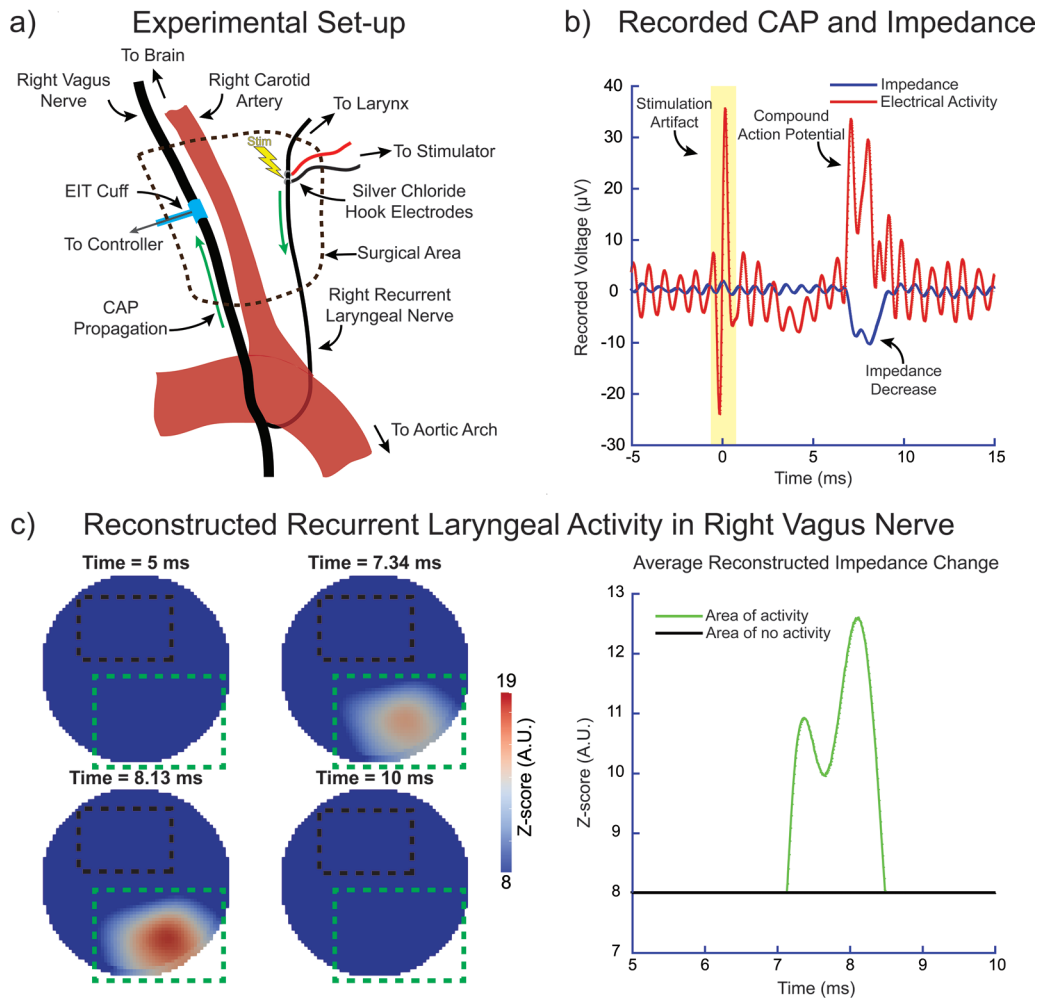
Figure 7. (a) Schematic showing the implantation and experimental set-up for recording *in vivo* EIT images of stimulated compound activity from the recurrent laryngeal nerve in the vagus nerve. (b) Recorded electrical activity (red) which comprises a stimulation artifact (yellow highlight) and compound action potential of the recurrent laryngeal nerve, as well as the recorded impedance change (blue) corresponding to the compound neural activity. (c) Reconstructed EIT images of the vagus nerve during recurrent laryngeal stimulation show a change in impedance due to the passing neural activity. Analysis of the average volume conductance of the time course reconstructions show a direct correlation between the recorded impedance decrease and the images.

animals with three trials in each animal. Although not investigated here, the localization power of this technique could be pushed further by varying the stimulation parameters to recruit only specific populations of neurons. The alteration of stimulation parameters and patterns is currently under more investigation for more fully characterizing EIT localization effectiveness.

One of the major challenges in recording electrical activity from peripheral nerves is the temporal dispersion of action potentials within the nerve [15]. Dispersion is caused by differences in the action potential propagation velocities, primarily due to fiber size and myelination which causes a temporal broadening of the perceived electrical activity and thus a decrease in maximum amplitude. One major benefit of EIT in this scenario is that although the maximum recorded amplitude of the nerve electrical activity decreases, the recorded impedance decrease is in theory proportional to the number of opened ion channels and thus the signal should not require visible compound activity to see an impedance change. This effect was well characterized for C-fibers using

a Hodgin–Huxley model in a recently published manuscript from Tarotin *et al* [44], however the effect at the Nodes of Ranvier have yet to be investigated in this method. As the challenge of imaging highly dispersed activity in the peripheral nervous system limits the application of devices relying solely on measuring action potentials within the nerve, the potential for this technique to image dispersed evoked activity in fast conducting fibers put it in the unique position to enable crucial feedback to many bioelectronic systems. However, more in-depth analysis of EIT data from highly dispersed motor fibers remains to be performed.

Conclusions

In this study we have demonstrated a simple technique for the fabrication of silicone embedded electrode arrays from stainless-steel foils, the subsequent application of multiple nanostructured materials, and the efficacy of these electrode arrays as neural cuffs for use in imaging compound activity via EIT. Electroplated platinum, iridium oxide, and PEDOT:pTS

coatings were evaluated for their performance in EIT accuracy with reconstructing a large impedance change (i.e. pin phantom) and their electrochemical properties such as real impedance and phase shift. Taking into account the ease of deposition and the overall performance of the EIT reconstructions PEDOT:pTS was identified as the best electrode coating for EIT of nervous tissue due to low impedance, improved location accuracy of the reconstruction, as well as reduced phase lag between recording electrodes during current injection. The efficacy of the optimized PEDOT:pTS coated neural cuffs was then shown through the recording of compound activity of the right recurrent laryngeal nerve in an *in vivo* setting. Utilizing the PEDOT:pTS neural cuff, highly dispersed compound activity corresponding to a stimulation of the right recurrent laryngeal nerve was imaged and selectively localized with EIT in the right cervical vagus nerve. This result demonstrates a potential avenue for the specific localization of highly dispersed compound action potential activity through the application of EIT with optimized electrode materials. Future work quantifying the distance of dispersion that EIT can overcome in both evoked and physiological activity is currently underway in our group. Overall, this work has identified PEDOT:pTS as a promising *in vivo* electrode material for use in EIT imaging of fast neural activity in the peripheral nervous system.

Acknowledgments

ORCID iDs

Christopher A R Chapman ● https://orcid.org/0000-0002-9009-0139
Kirill Aristovich ● https://orcid.org/0000-0002-2924-5680
James Avery ● https://orcid.org/0000-0002-4015-1802

References

[1] Lacour S P, Courtine G and Guck J 2016 Materials and technologies for soft implantable neuroprostheses *Nat. Rev. Mater.* **1** 16063
[2] Tybrandt K, Stauffer F and Vörös J 2016 Multilayer patterning of high resolution intrinsically stretchable electronics *Sci. Rep.* **6** 25641
[3] Tybrandt K and Voeroes J 2016 Fast and efficient fabrication of intrinsically stretchable multilayer circuit boards by wax pattern assisted filtration *Small* **12** 180–4
[4] Martinez V, Stauffer F, Adagunodo M O, Forro C, Vörös J and Larmagnac A 2015 Stretchable silver nanowire-elastomer composite microelectrodes with tailored electrical properties *ACS Appl. Mater. Interfaces* **7** 13467–75
[5] Kim D-H and Rogers J A 2008 Stretchable electronics: materials strategies and devices *Adv. Mater.* **20** 4887–92
[6] Rogers J A, Someya T and Huang Y 2010 Materials and mechanics for stretchable electronics *Science* **327** 1603–7
[7] Blau A, Murr A, Wolff S, Sernagor E, Medini P, Iurilli G, Ziegler C and Benfenati F 2011 Flexible, all-polymer microelectrode arrays for the capture of cardiac and neuronal signals *Biomaterials* **32** 1778–86
[8] Yu Z, Graudejus O, Tsay C, Lacour S P, Wagner S and Morrison B 2009 Monitoring hippocampus electrical activity *in vitro* on an elastically deformable microelectrode array *J. Neurotrauma* **26** 1135–45
[9] Kuzum D, Takano H, Shim E, Reed J C, Juul H, Richardson A G, de Vries J, Bink H, Dichter M A, Lucas T H, Coulter D A, Cubukcu E and Litt B 2014 Transparent and flexible low noise graphene electrodes for simultaneous electrophysiology and neuroimaging *Nat. Commun.* **5** 5259
[10] Ware T, Simon D, Arreaga-Salas D E, Reeder J, Rennaker R, Keefer E W and Voit W 2012 Fabrication of responsive, softening neural interfaces *Adv. Funct. Mater.* **22** 3470–9
[11] Minev I R *et al* 2015 Biomaterials. Electronic dura mater for long-term multimodal neural interfaces *Science* **347** 159–63
[12] Schiefer M A, Polasek K H, Triolo R J, Pinault G C J and Tyler D J 2010 Selective stimulation of the human femoral nerve with a flat interface nerve electrode *J. Neural Eng.* **7** 026006
[13] Navarro X, Krueger T B, Lago N, Micera S, Stieglitz T and Dario P 2005 A critical review of interfaces with the peripheral nervous system for the control of neuroprostheses and hybrid bionic systems *J. Peripher. Nerv. Syst.* **10** 229–58
[14] Peltonen S, Alanne M and Peltonen J 2013 Barriers of the peripheral nerve *Tissue Barriers* **1** e24956
[15] Olney R K, Budingen H J and Miller R G 1987 The effect of temporal dispersion on compound action potential area in human peripheral nerve *Muscle Nerve* **10** 728–33
[16] Aristovich K, Donegá M, Blochet C, Avery J, Hannan S, Chew D J and Holder D 2018 Imaging fast neural traffic at fascicular level with electrical impedance tomography: proof of principle in rat sciatic nerve *J. Neural Eng.* **15** 056025
[17] Holder D 2004 *Introduction to Biomedical Electrical Impedance Tomography* (London: Taylor and Francis)
[18] Riera J, Riu P J, Casan P and Masclans J R 2011 Electrical impedance tomography in acute lung injury *Med. Intensiva* **35** 509–17
[19] Vongerichten A N, Santos dos G S, Aristovich K, Avery J, McEvoy A, Walker M and Holder D S 2016 Characterisation and imaging of cortical impedance changes during interictal and ictal activity in the anaesthetised rat *NeuroImage* **124** 813–23
[20] Aristovich K Y, Packham B C, Koo H, Santos dos G S, McEvoy A and Holder D S 2016 Imaging fast electrical activity in the brain with electrical impedance tomography *NeuroImage* **124** 204–13
[21] Aristovich K Y, Santos dos G S, Packham B C and Holder D S 2014 A method for reconstructing tomographic images of evoked neural activity with electrical impedance tomography using intracranial planar arrays *Physiol. Meas.* **35** 1095–109
[22] Cogan S F 2008 Neural stimulation and recording electrodes *Annu. Rev. Biomed. Eng.* **10** 275–309
[23] Chapman C A R, Goshi N and Seker E 2017 Multifunctional neural interfaces for closed-loop control of neural activity *Adv. Funct. Mater.* **4** 1703523

[24] Hu J, Abdelsalam M, Bartlett P, Cole R, Sugawara Y, Baumberg J, Mahajan S and Denuault G 2009 Electrodeposition of highly ordered macroporous iridium oxide through self-assembled colloidal templates *J. Mater. Chem.* **19** 3855–8

[25] Avery J, Dowrick T, Faulkner M, Goren N and Holder D 2017 A versatile and reproducible multi-frequency electrical impedance tomography system *Sensors* **17** 280

[26] Jehl M, Dedner A, Betcke T, Aristovich K, Klöfkorn R and Holder D 2015 A fast parallel solver for the forward problem in electrical impedance tomography *IEEE Trans. Biomed. Eng.* **62** 126–37

[27] Adler A *et al* 2009 GREIT: a unified approach to 2D linear EIT reconstruction of lung images *Physiol. Meas.* **30** S35–55

[28] Staples N A, Goding J A, Gilmour A D, Aristovich K Y, Byrnes-Preston P, Holder D S, Morley J W, Lovell N H, Chew D J and Green R A 2018 Conductive hydrogel electrodes for delivery of long-term high frequency pulses *Frontiers Neurosci.* **11** 204

[29] Uludag M, Aygun N and Isgor A 2016 Motor function of the recurrent laryngeal nerve: sometimes motor fibers are also located in the posterior branch *Surgery* **160** 153–60

[30] Fleming J C, Gibbins N, Ingram P J and Harries M 2011 An anatomical study of the myelination of human laryngeal nerves *J. Laryngol. Otol.* **125** 1263–7

[31] Schuettler M, Schroeer S, Ordonez J S and Stieglitz T 2011 Laser-fabrication of peripheral nerve cuff electrodes with integrated microfluidic channels *2011 5th Int. IEEE/EMBS Conf. on Neural Engineering (IEEE)* pp 245–8

[32] Schuettler M, Koch K P, Stieglitz T, Scholz O, Haberer W, Keller R and Meyer J U 2000 Multichannel neural cuff electrodes with integrated multiplexer circuit *1st Annual Int. IEEE-EMBS Special Topic Conf. on Microtechnologies in Medicine and Biology. Proc. (Cat. No.00EX451)* (IEEE) pp 624–9

[33] Green R A, Matteucci P B, Dodds C W D, Palmer J, Dueck W F, Hassarati R T, Byrnes-Preston P J, Lovell N H and Suaning G J 2014 Laser patterning of platinum electrodes for safe neurostimulation *J. Neural Eng.* **11** 056017

[34] Pine J 1980 Recording action potentials from cultured neurons with extracellular microcircuit electrodes *J. Neurosci. Methods* **2** 19–31

[35] Ilic B, Czaplewski D, Neuzil P, Stanczyk T, Blough J and Maclay G J 2000 Preparation and characterization of platinum black electrodes *J. Mater. Sci.* **35** 3447–57

[36] Kim Y H, Kim G H, Kim M S and Jung S-D 2016 Iridium oxide–electrodeposited nanoporous gold multielectrode array with enhanced stimulus efficacy *Nano Lett.* **16** 7163–8

[37] Cogan S F, Plante T D and Ehrlich J 2004 Sputtered iridium oxide films (SIROFs) for low-impedance neural stimulation and recording electrodes *Conf. Proc. IEEE Eng. Med. Biol. Soc.* vol **6** pp 4153–6

[38] Green R and Abidian M R 2015 Conducting polymers for neural prosthetic and neural interface applications *Adv. Mater. Weinheim* **27** 7620–37

[39] Cogan S F, Ehrlich J, Plante T D, Smirnov A, Shire D B, Gingerich M and Rizzo J F 2009 Sputtered iridium oxide films for neural stimulation electrodes *J. Biomed. Mater. Res.* B **89** 353–61

[40] Tyler D J and Durand D M 2002 Functionally selective peripheral nerve stimulation with a flat interface nerve electrode *IEEE Trans. Neural Syst. Rehabil. Eng.* **10** 294–303

[41] Aristovich K Y, Santos Dos G S and Holder D S 2015 Investigation of potential artefactual changes in measurements of impedance changes during evoked activity: implications to electrical impedance tomography of brain function *Physiol. Meas.* **36** 1245–59

[42] Warman E N, Grill W M and Durand D 1992 Modeling the effects of electric fields on nerve fibers: determination of excitation thresholds *IEEE Trans. Biomed. Eng.* **39** 1244–54

[43] Whitwam J G 1976 Classification of peripheral nerve fibres. An historical perspective *Anaesthesia* **31** 494–503

[44] Tarotin I, Aristovich K and Holder D 2018 Model of impedance changes in unmyelinated nerve fibres *IEEE Trans. Biomed. Eng.* (https://doi.org/10.1109/TBME.2018.2849220)